ACS Catalysis

Research Article

pubs.acs.org/acscatalysis

Simultaneous NO_x and Particulate Matter Removal from Diesel Exhaust by Hierarchical Fe-Doped Ce−Zr Oxide

Ying Cheng,[†,⊥] Weiyu Song,[†,‡,⊥] Jian Liu,[*,†] Huiling Zheng,[†] Zhen Zhao,[*,§] Chunming Xu,[†] Yuechang Wei,[†] and Emiel J. M. Hensen[*,‡]

[†]State Key Laboratory of Heavy Oil Processing, China University of Petroleum, 18 Fuxue Road, Chang Ping, Beijing 102249, China

[‡]Schuit Institute of Catalysis, Department of Chemical Engineering and Chemistry, Eindhoven University of Technology, P.O. Box 513, 5600 MB Eindhoven, The Netherlands

[§]Institute of Catalysis for Energy and Environment, Shenyang Normal University, Shenyang 110034, China

Supporting Information

ABSTRACT: Particulate matter and NO_x emissions from diesel exhaust remains one of the most pressing environmental problems. We explore the use of hierarchically ordered mixed Fe−Ce−Zr oxides for the simultaneous capture and oxidation of soot and reduction of NO_x by ammonia in a single step. The optimized material can effectively trap the model soot particles in its open macroporous structure and oxidize the soot below 400 °C while completely removing NO in the 285−420 °C range. Surface characterization and DFT calculations emphasize the defective nature of Fe-doped ceria. The isolated Fe ions and associated oxygen vacancies catalyze facile NO reduction to N_2. A mechanism for the reduction of NO with NH_3 on Fe-doped ceria is proposed involving adsorbed O_2. Such adsorbed O_2 species will also contribute to the oxidation of soot.

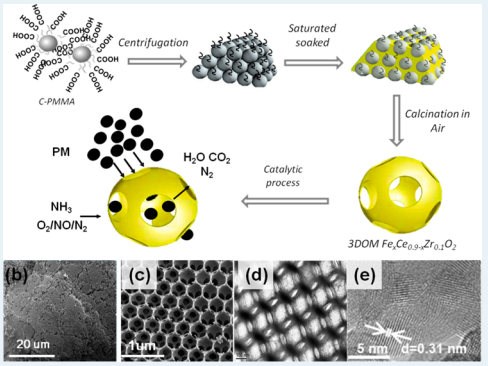

KEYWORDS: *soot oxidation, NO_x reduction, ceria, doping, macropores*

INTRODUCTION

Air pollution caused by exhaust gas emissions from various modes of transportation carries significant risk for human health and the environment.[1−4] Introduced in the 1970s, the three-way catalytic convertor has become a widespread technology for removing noxious gases from gasoline-fueled cars.[5] Precious group metals (PGMs) dispersed as nanoparticles on suitable oxide support materials can simultaneously oxidize CO and hydrocarbons and reduce NO_x to less harmful gases. This technology cannot be used to remove NO_x from the exhaust of diesel engines because it is too rich in oxygen. Aside from NO_x, diesel exhaust remains a major contributor to undesirable emissions of particulate matter (PM). Soot particles pose the most serious threat to human health. The major challenge in diesel exhaust cleanup is the removal of NO_x under lean (oxygen-rich) conditions.[6,7] Yoshida et al. were the first to propose the simultaneous removal of PM and NO_x by a single catalytic material.[8] Significant efforts have been made to develop suitable catalysts for this purpose.[9] Current commercial solutions combine a diesel oxidation catalyst (DOC) for the removal of CO and hydrocarbons, a catalyzed diesel particulate filter (CDPF) for soot filtration, and a selective catalytic reduction (SCR) step to remove NO_x using a reducing gas such as ammonia. These operations are carried out in different compartments, thereby increasing the size and cost of this technology. Another drawback is that in some steps expensive PGMs such as Pt are important catalyst ingredients.[10,11] Consequently, there is significant incentive to develop novel approaches that rely on more abundant elements and combine one or more pollutant conversion steps.[12]

A potential alternative is to combine the CDPF and SCR functions in a selective catalytic reduction and particulate filter (SCRPF). The particular challenge here is to achieve a high rate of soot oxidation in combination with substantial NO_x reduction at sufficiently low temperature. Therefore, it is necessary to identify materials with suitable redox abilities. Candidate materials are (mixed) metal oxides,[13,14] hydrotalcites,[15] and alkali oxides.[16] Besides high activity, increasing the contact area between the catalysts and solid reactant is a particular challenge in this field.[17,18] It is also important that the texture of these materials be suitable for capturing soot particles, which are typically larger than 25 nm. In such case, hierarchically structured oxides may be considered. Three-dimensionally ordered macroporous (3DOM) materials offer an ordered, interconnected macroporous structure with openings suitable for the capture of soot particles.[19]

Ceria is well-known for its excellent oxygen storage capacity.[20,21] The problem of low high-temperature stability of ceria structures can be overcome by introducing foreign elements into the ceria lattice, which also improves its redox

Received: November 29, 2016
Revised: April 22, 2017
Published: April 26, 2017

DOI: 10.1021/acscatal.6b03387
ACS Catal. 2017, 7, 3883−3892

properties.[22−25] For instance, Ce−Zr mixed oxides have been explored in the context of NO_x reduction and soot oxidation.[26−32] Other reports have already shown that doping Fe into ceria improves its reducibility, leading to more facile generation of oxygen vacancies at the surface important for soot oxidation and NO_x reduction.[33,34]

Herein, we report for the first time an Fe-doped 3DOM mixed Ce−Zr oxide material that can simultaneously remove PM and NO_x from diesel exhaust. Ammonia is used as a reductant for NO_x. We prepared the 3DOM mixed oxides by a carbon-templating method and varied the Fe content in the mixed oxide. Optimized materials show good performance in simultaneous removal of soot and NO_x at intermediate temperatures. The 3DOM mixed oxides are thermally stable and can be repeatedly regenerated without loss of activity. Density functional theory (DFT) calculations have been performed to understand the surface reducibility of the mixed oxides and gain insight into the role of Fe and surface oxygen vacancies in the reaction mechanism of NO_x reduction and soot oxidation.

EXPERIMENTAL SECTION

Materials Synthesis. All starting chemicals were purchased from Sigma-Aldrich and used without further purification. Carboxy-modified poly(methyl methacrylate) (c-PMMA) spheres were prepared by a modified emulsifier-free biphasic emulsion polymerization technique using initiators for the water and oil phase.[35−37] Methyl methacrylate (MMA, 99%) was the monomer used for obtaining PMMA spheres. Addition of acrylic acid (AA, >99%) monomer to the mixture allowed for introducing carboxyl groups in the PMMA. Briefly, a four-necked, 1000 mL round-bottomed flask was filled a mixed solution of acetone (80 mL, >98%), distilled water (240 mL), and the monomers (120 mL). The resulting mixture was heated to 80 °C by a hot water bath. After approximately 30 min, 0.6 g of potassium persulfate (KPS, water-phase initiator, >99%) and 0.15 g of azodiisobutyronitrile (AIBN, oil-phase initiator, 98%) mixed with 40 mL of distilled water (preheated to 80 °C) were added. The whole solution was stirred at a constant speed of 350 min^{-1} for approximately 2 h with N_2 bubbling. The obtained latex was cooled to room temperature and then centrifuged. The solid material was dried at room temperature (c-PMMA).

Three-dimensionally ordered macroporous (3DOM) $Ce_{0.9-x}Fe_xZr_{0.1}O_2$ catalysts were prepared by carboxy-modified colloidal crystal templating (CMCCT). $Ce(NO_3)_3{\cdot}6H_2O$ (99.5%), $Fe(NO_3)_3{\cdot}9H_2O$ (99.99%), and $ZrOCl_2{\cdot}8H_2O$ (98%) were used as precursors for obtaining mixed metal oxides. Suitable amounts of $Ce(NO_3)_3{\cdot}6H_2O$, $Fe(NO_3)_3{\cdot}9H_2O$ and $ZrOCl_2{\cdot}8H_2O$ were first dissolved in a mixture of ethylene glycol and methanol followed by vigorous stirring for 40 min. Then, this solution was contacted with the c-PMMA hard template for 12 h. After impregnation, the final material was subjected to vacuum filtration to remove excess precursor solution. The precipitate was dried at 50 °C in a vacuum oven, calcined in inert (Ar) atmosphere at 130 °C for 1 h, followed by increasing the temperature to 600 °C at a rate of 1 °C/min. After a dwell time of 5 h, the atmosphere was changed to air, and the sample was kept at 600 °C for another 3 h. The first step in Ar pyrolyzes the carbon: the sp^2-hybridized carbon atoms are converted to a sturdy amorphous carbon material, which acts as the hard template for the in situ formation of the 3DOM mixed oxide. The carbon template was finally removed by calcination in air.

Catalyst Characterization. The crystal structure of the samples was investigated by powder X-ray diffraction (XRD) spectrometer (Shimadzu XRD 6000) with Cu Kα radiation (0.02° intervals in the range 5−90° at a rate of 4°/min). Nitrogen adsorption isotherms were measured using a Micromeritics TriStar-II 3020 instrument. SEM (FEI Quanta200F) was conducted to analyze the surface morphology of the samples. The microstructure and lattice parameters were analyzed by TEM (JEOL JEM 2100 electron microscope). Raman spectra were collected in the anti-Stokes range of 100−2000 cm^{-1} using an inVia Reflex-Renishaw spectrometer. The sample was excited using a He−Gd laser (532 nm excitation wavelength). X-ray photoelectron spectra were measured on an XPSPHI-1600 ESCA spectrometer using an Al Kα anode ($h\nu$ = 1253.6 eV) as the X-ray source and using C 1s at 284.6 eV as an internal binding energy standard. Temperature-programmed desorption of ammonia (NH_3-TPD) was carried out in a conventional flow apparatus using a thermal conductivity detector. Temperature-programmed reduction with H_2 (H_2-TPR) measurements was performed in an Autosorb IQ Quantachrome apparatus.

Catalytic Activity Measurements. Catalytic activity measurements were taken in a fixed-bed reactor. Printex U carbon black (Orion Engineered Carbons) was used as a model for particulate matter. This carbon black has an average particle size of 25 nm and surface area of 100 m^2/g. Prior to each catalytic activity test, 100 mg of catalyst and 10 mg of Printex U were mixed gently with a spatula (loose contact mode). Thereafter, the mixture was placed between quartz wool plugs in a quartz tubular reactor with an inner diameter of 10 mm. The reactor feed was comprised of 1000 ppm of NO, 1000 ppm of NH_3, and 3% O_2 with N_2 as the balance gas. In some cases, 5% H_2O was added to the reactor feed to evaluate the influence of moisture. The gas hourly space velocity (GHSV) was 25,000 h^{-1} with a total flow of 100 mL/min at standard pressure and temperature. The performance of the optimum catalyst was also evaluated at higher GHSV by decreasing the catalyst amount. The concentrations of NH_3, NO, NO_2, N_2O, CO_2, and CO were monitored at the outlet by online infrared spectroscopy (Thermo Is50 FTIR equipped with a 2.4 m gas cell). For quantification, a robust method for multicomponent gas analysis was used implementing TQ Analyst software and making use of calibration curves based on mixtures of the relevant gases in different concentration ranges.[38] Before each catalytic activity measurement, the catalyst sample was first swept by a flow of 100 mL/min N_2 for approximately 45 min prior to collecting a background IR spectrum of the reactor effluent. Afterward, effluent IR spectra were recorded of the reactor feed consisting of 1000 ppm of NH_3, 1000 ppm of NO, and 3% O_2 in N_2 for 30 min. Catalytic activity tests were carried out by heating the reactor bed from 30 to 600 °C at a rate of 3 °C/min. The stability of the catalyst was evaluated by repeatedly evaluating its performance in this manner. For this purpose, 10 mg of Printex U was mixed with the catalyst bed. The absence of mass transfer limitations for the NO reduction reaction was verified by applying the Koros−Nowak criterion, and the absence of heat transfer due to soot oxidation was evaluated by Mears' criteria (see the Supporting Information).

Computational Methods. DFT calculations were performed using the VASP code employing the GGA-PBE exchange-correlation potential.[39] The valence electrons (5s,

DOI: 10.1021/acscatal.6b03387
ACS Catal. 2017, 7, 3883−3892

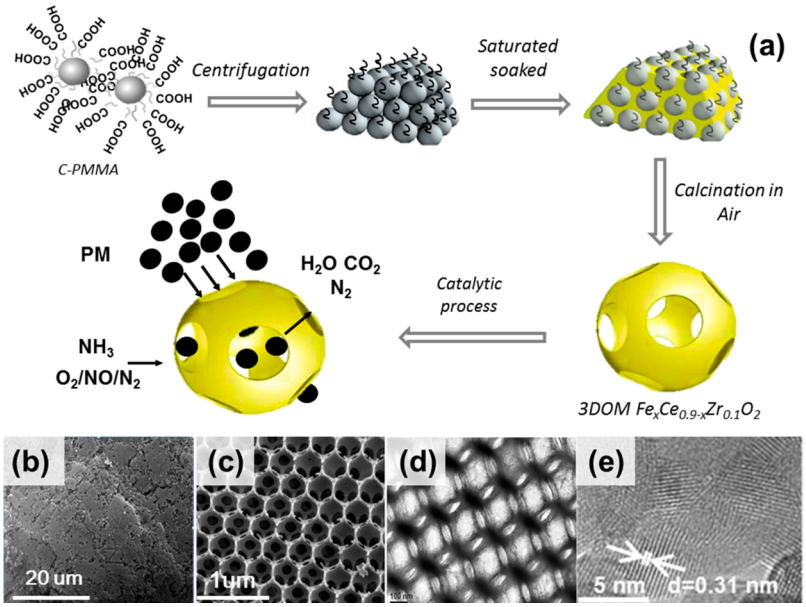

Figure 1. (a) Schematic representation of the synthesis of the 3DOM mixed Ce−Fe−Zr oxide and its catalytic function in diesel exhaust cleanup; (b) SEM and (c−e) TEM images at different magnifications showing the macroporous structure (c, d) and d-spacing of CeO_2(111).

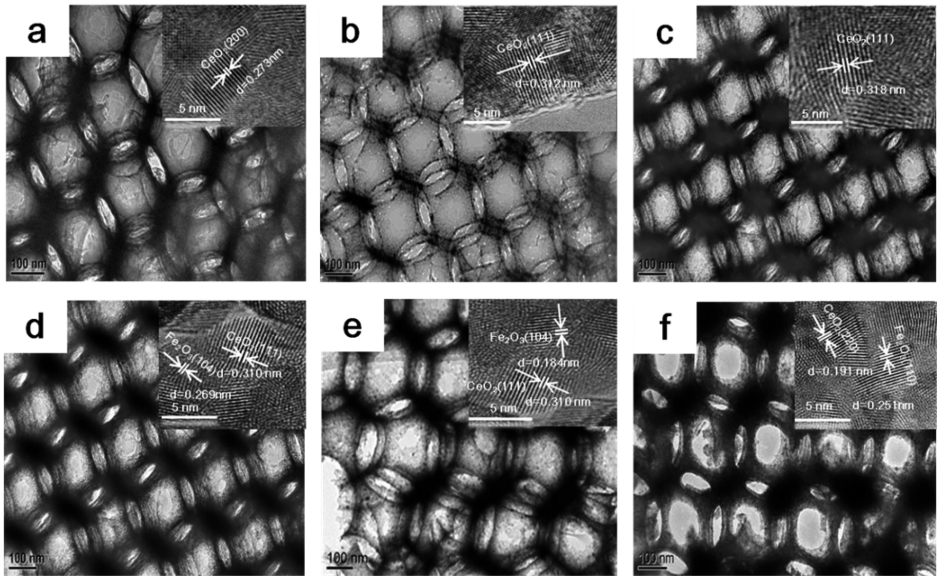

Figure 2. Representative TEM images of 3DOM materials: (a) CeO_2, (b) $Ce_{0.85}Fe_{0.05}Zr_{0.1}O_2$, (c) $Ce_{0.8}Fe_{0.1}Zr_{0.1}O_2$, (d) $Ce_{0.7}Fe_{0.2}Zr_{0.1}O_2$, (e) $Ce_{0.6}Fe_{0.3}Zr_{0.1}O_2$, and (f) $Ce_{0.5}Fe_{0.4}Zr_{0.1}O_2$.

4f, 3d for Ce; 2s, 2p for O; and 4s, 3d for Fe) were expanded in a plane-wave basis set with a cutoff energy of 400 eV. The projector augmented wave method (PAW) was used to describe the effect of core electrons.[40,41] The bulk equilibrium lattice constant of ceria (5.49 Å) previously calculated by PBE + U (U_{eff} = 4.5 eV) was uSed.[42] Then, a 3 × 3 surface unit cell was used for the CeO_2 (111) surface. Fe atoms and the six top atomic layers of the ceria slab were allowed to relax, whereas the three bottom layers were kept fixed to their bulk positions. The vacuum gap thickness was set to 15 Å. Because of the large size of the slab model (11.64 Å × 11.64 Å), a Monkhorst pack 1 × 1 × 1 mesh was used for Brillouin zone integration. All structures were relaxed until the forces acting on each atom were smaller than 0.05 eV/Å. To improve the description of the on-site Coulomb interactions in the Ce-f states and Fe-d states, a Hubbard correction was added. For Ce, a value of U_{eff} = 4.5 eV was used for its 4f orbital.[43−45] For Fe, a value of U_{eff} = 3.8 eV was used for its 3d orbital.[46] The location and energy of transition states were calculated with the climbing-image nudged elastic band method (CINEB).[47] Adsorption energies are expressed with reference to the adsorbing molecule in vacuum. The energies of all gas species were determined in a 15 Å cubic box with a cutoff energy of 400 eV at the Γ-point.

RESULTS AND DISCUSSION

Preparation and Characterization. The carboxy-modified variation of colloidal crystal templating using poly(methyl methacrylate) (c-PMMA) spheres is schematically depicted in Figure 1.[35] The sturdy amorphous carbon material derived from PMMA pyrolysis can be used as a hard template for the

DOI: 10.1021/acscatal.6b03387
ACS Catal. 2017, 7, 3883−3892

fabrication of structured metal oxides.[48] The carboxy modification of PMMA using acrylic acid as a comonomer was necessary to obtain a well-mixed Ce−Zr oxide structure. We prepared c-PMMA spheres by copolymerization of MMA and AA using suitable initiators. Centrifuging and drying of the latex resulted in a highly ordered c-PMMA material. The structured oxides were obtained by impregnation of the solid organic template with a mixture of suitable precursor salts dissolved in a mixture of ethylene glycol and methanol followed by pyrolysis at 600 °C in inert and calcination in air to remove the organic part. TEM images show the ordered texture of the optimum $Ce_{0.8}Fe_{0.1}Zr_{0.1}O_2$ mixed oxide with macropores and uniformly sized walls (Figure 1b−d) interconnected by smaller windows.[49] All materials have the fluorite structure of ceria independent of the Fe and Zr content, and no separate iron or zirconium oxide phases were detected by XRD (Figure S2). Small shifts in the main diffraction peaks for the mixed oxides compared to CeO_2 evidence inclusion of Fe^{3+} and Zr^{4+} into the fluorite structure of ceria. High-resolution TEM images show (111) surface terminations with the d-spacing being consistent with that of ceria (Figure 1e).

Introduction of Fe and Zr into the CeO_2 lattice did not alter the 3DOM structure as long as the Fe substitution level was kept below 0.2 (Figures S3 and S4). Introduction of more Fe led to segregated iron oxides observable in high-resolution TEM images (Figure 2).[50] Raman spectra of the 3DOM $Ce_{0.9-x}Fe_xZr_{0.1}O_2$ samples contain an absorption band at ∼460 cm^{-1} due to the F_{2g} mode of CeO_2 (Figure 3).[24,51] Only at

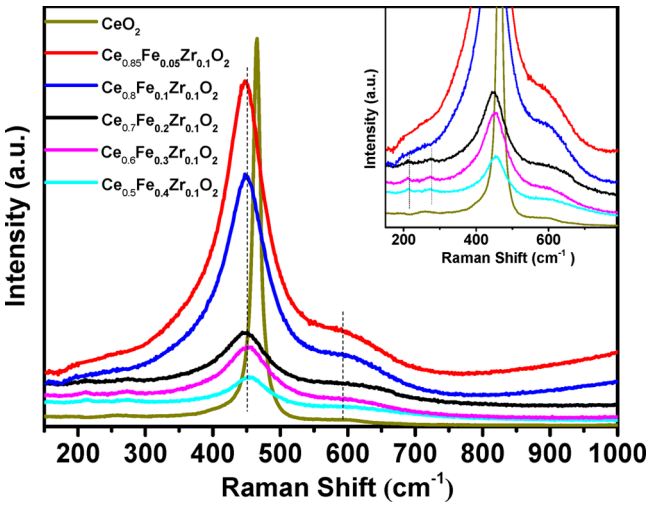

Figure 3. Raman spectra of the of 3DOM materials: (a) CeO_2, (b) $Ce_{0.85}Fe_{0.05}Zr_{0.1}O_2$, (c) $Ce_{0.8}Fe_{0.1}Zr_{0.1}O_2$, (d) $Ce_{0.7}Fe_{0.2}Zr_{0.1}O_2$, (e) $Ce_{0.6}Fe_{0.3}Zr_{0.1}O_2$, and (f) $Ce_{0.5}Fe_{0.4}Zr_{0.1}O_2$.

higher Fe content ($x \geq 0.2$) did Raman bands at 215 and 280 cm^{-1} typical of Fe−O stretching vibrations in Fe oxides appear. The nitrogen adsorption−desorption isotherms show a nearly linear correlation between the relative pressure and absorbed volume (Figure S4), which is the consequence of unrestricted monolayer-multilayer adsorption. The presence of an H3 hysteresis loop is further indication of the macroporous structure. Although the pure ceria material has a surface area of approximately 12 m^2/g (Table S1), the mixed oxides have higher surface area, which is in part due to the presence of mesopores evident from the hysteresis in the p/p_0 range between 0.4 and 0.8. These mesopores are likely occluded in the walls of the macroporous material.

Catalytic Activity Measurements. Compared with ceria, mixed Ce−Zr oxides display better thermal stability and oxygen storage capacity, which is beneficial for PM combustion.[52] In general, it is a challenge to reduce NO_x under the oxygen-rich conditions required to oxidize PM into CO_2.[53] As NO_2 is more effective in soot oxidation than O_2, soot is usually first oxidized in the NO_x/O_2 exhaust gas, followed by ammonia-assisted NO_x reduction using, for instance, Cu/zeolites placed downstream of the PM combustion zone.[54−57] Ammonia can be conveniently supplied to the after-treatment system by hydrolyzing urea. It has been demonstrated before that Fe is an active ingredient for NO_x reduction.[58]

We optimized the Fe and Zr content of the 3DOM mixed Fe−Ce−Zr oxide toward low-temperature NO_x reduction and complete soot oxidation. For this purpose, model soot particles with an average size of 25 nm were loosely mixed with the 3DOM mixed oxide catalysts and exposed to a simulated diesel exhaust feed containing 1000 ppm of NO, 1000 ppm of NH_3, and 3% O_2 with balance N_2 fed at a GHSV of 25,000 h^{-1}. The loose contact mode provides a better approximation of soot trapping in a DPF than tight contact conditions involving grinding the components in a mortar.[7] Figure 4 shows the transient behavior of the catalyst during temperature-programmed reaction. CO_2 is produced by combustion of the model soot particles. The effluent CO_2 concentration decreases at high temperature, as combustion of the model soot near completion. NO conversion at high temperature is limited because of the oxidation of NH_3 (Figure S5). In low temperature NH_3−SCR, NO oxidation to NO_2 is crucial to improve the rate of NO_x removal via the fast SCR reaction.[59,60] Moreover, NO_2 is also a more active soot oxidant than NO.[61] The 3DOM $Ce_{0.8}Fe_{0.1}Zr_{0.1}O_2$ catalyst shows excellent activity in the oxidation of NO to NO_2 (Figure S6). The optimal catalyst $Ce_{0.8}Fe_{0.1}Zr_{0.1}O_2$ is effective for reducing NO by 90% in the range of 265−420 °C and for completely oxidizing soot to CO_2 at approximately 375 °C. Among the 3DOM mixed Fe−Ce−Zr−O catalysts (Table 1), the optimized material is able to oxidize coke below 400 °C. When the Fe content is too high, the performance was much lower because segregated Fe oxides block the surface of the solid Fe−Ce−Zr−O solution.[62] Consistent with this, Fe_2O_3 itself showed low activity in PM oxidation and NO_x SCR.

We also evaluated the performance of the catalyst in the presence of water. Adding 5% H_2O to the reactor feed, the catalytic performance for PM oxidation was decreased, whereas that for NO_x reduction was only slightly lower in comparison to the experiments without water (Figure S7). Complete reduction of NO was achieved in the 343−426 °C range, and soot was completely combusted at 421 °C. Clearly, water had a negative effect on low-temperature NO conversion but improved NO reduction rate at high temperature. The strong influence of water on NO reduction is due to competitive adsorption of NH_3 and H_2O. This limits NH_3 adsorption on acid sites at low temperature, thus decreasing low temperature NO_x reduction. On the other hand, at high temperature, the inhibiting effect of H_2O slows NH_3 oxidation, resulting in a higher NO_x reduction rate.

As the used space velocity was relatively low with respect to diesel exhaust gas treatment, we also evaluated the performance of the optimum 3DOM $Ce_{0.8}Fe_{0.1}Zr_{0.1}O_2$ at higher space velocities (GHSV of 50,000 and 100,000 h^{-1}). Figure S8 shows

DOI: 10.1021/acscatal.6b03387
ACS Catal. 2017, 7, 3883−3892

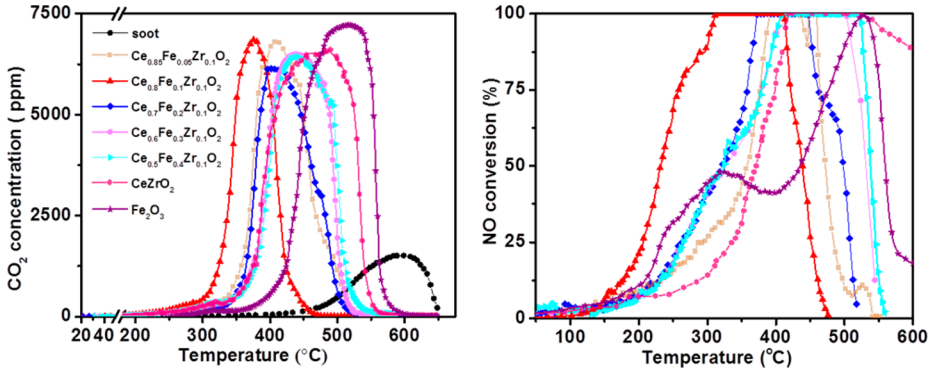

Figure 4. (left) CO_2 concentration and (right) NO conversion as a function of temperature upon exposure of 3DOM $Ce_{0.9-x}Fe_xZr_{0.1}O_2$ catalysts loosely mixed with model soot particles in a gas feed containing 1000 ppm of NH_3, 1000 ppm of NO, 3% O_2 and balance N_2 at a gas hourly space velocity of 25,000 h^{-1}.

Table 1. Performance of Structured Oxides in Simultaneous NO_x Reduction and PM Combustion[a]

catalyst	T_{max,CO_2}[b] (°C)	$T_{max,NO}$[c] (°C)
Fe_2O_3	514	526
$CeZrO_2$	477	418−523
$Ce_{0.85}Fe_{0.05}Zr_{0.1}O_2$	398	387−438
$Ce_{0.8}Fe_{0.1}Zr_{0.1}O_2$	375	285−410
$Ce_{0.7}Fe_{0.2}Zr_{0.1}O_2$	409	372−448
$Ce_{0.6}Fe_{0.3}Zr_{0.1}O_2$	433	404−510
$Ce_{0.5}Fe_{0.4}Zr_{0.1}O_2$	442	408−523

[a]Catalyst (100 mg) loosely mixed with 10 mg of Printex U model soot particles, 1000 ppm of NO, 1000 ppm of NH_3, and 3% O_2 and balance N_2 at a gas hourly space velocity of 25,000 h^{-1}. [b]Temperature of maximum CO_2 concentration. [c]Temperature range where NO conversion is complete.

that under these more stringent conditions catalytic performance was decreased. Complete NO_x conversion was still obtained in the 338−420 °C temperature range at a GHSV of 50,000 h^{-1}, whereas at the highest GHSV, the maximum NO conversion was limited to 80%. The PM combustion rate displayed maxima at 407 and 435 °C for GHSV values of 50,000 and 100,000 h^{-1}.

Figure 5 shows that the optimized 3DOM $Ce_{0.8}Fe_{0.1}Zr_{0.1}O_2$ catalyst can be reused without loss of activity for five consecutive cycles with fresh model soot being added after each cycle. Because the ceramic materials may be exposed to high temperatures in real applications, we also aged the optimum 3DOM mixed oxide at 900 °C in air for 5 h. This had only a minor effect on the catalytic performance (Figure S9) with the maximum rate of soot combustion being observed at 398 °C and full NO conversion in the 327−420 °C range. SEM shows that the texture of the 3DOM mixed oxide is largely retained, emphasizing its good thermal stability (Figure S10). Comparison of the catalytic performance of the optimum 3DOM catalyst to literature data emphasizes the outstanding performance in combined soot oxidation and NO reduction (Table S2). SEM images of the original and the catalyst used in five consecutive cycles demonstrates that the structured mixed oxide is thermally stable in the experiments (Figure 6).

Figure 5 also displays the performance of a nontemplated mixed oxide of the same composition as the optimal one. Soot combustion is delayed too much at higher temperatures, presumably because of the much less efficient contact of the soot particles with the surface of the mixed oxide. PM oxidation can enhance NO_x reduction by involving C═O groups on soot, which are intermediates in the complete oxidation of soot.[63] Compared with the large pores of the 3DOM structure, the average pore size of the nontemplated mixed oxide is only 15.8 nm, too small for the model soot particles to enter. Thus, the soot particles can only interact with a much smaller portion of the mixed oxide surface. The strong influence of the texture together with the use of the loose mixing method suggests that the model soot particles will enter the pores of the 3DOM structure during the performance test. This supposition is confirmed by studying a 3DOM sample that was only heated to 250 °C. Figure 6 shows TEM images of the model soot as well as a soot particle trapped in the large pores of the 3DOM

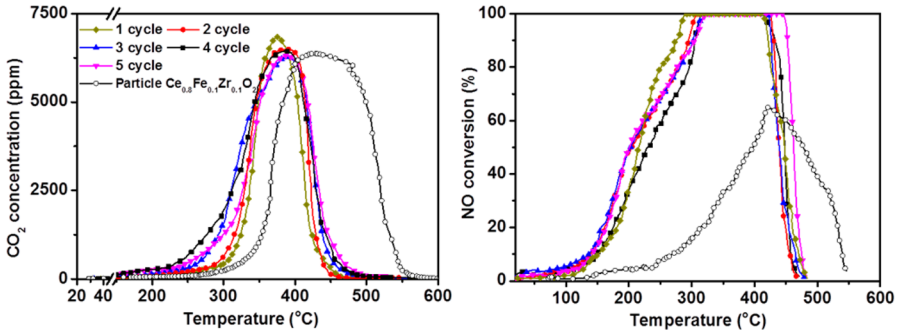

Figure 5. Reuse of the optimal 3DOM $Ce_{0.8}Fe_{0.1}Zr_{0.1}O_2$ catalyst during five consecutive cycles (the spent catalyst was mixed with new Printex U model soot particles and re-evaluated under similar conditions; GHSV = 25,000 h^{-1}, 1000 ppm of NH_3, 1000 ppm of NO, 3% O_2 in N_2, 0.1 model soot/catalyst mass ratio).

DOI: 10.1021/acscatal.6b03387
ACS Catal. 2017, 7, 3883−3892

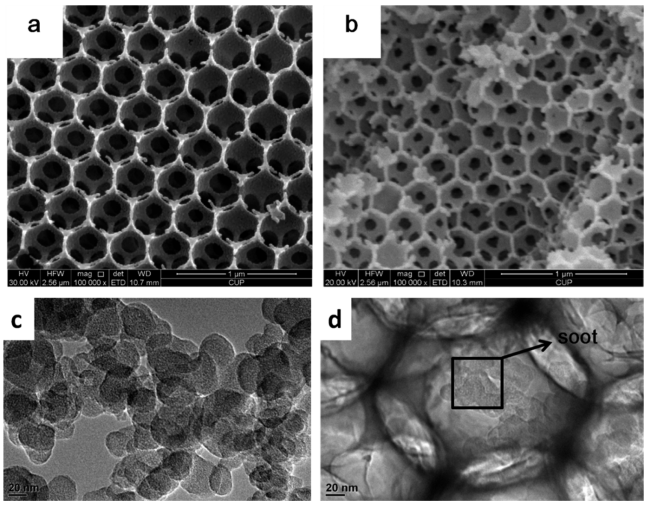

Figure 6. SEM of the (a) fresh and (b) spent optimal 3DOM $Ce_{0.8}Fe_{0.1}Zr_{0.1}O_2$ catalyst after five cycles; TEM images of (c) Printex U and (d) 3DOM $Ce_{0.8}Fe_{0.1}Zr_{0.1}O_2$ catalyst mixed with Printex U after temperature-programmed oxidation until 250 °C (reaction conditions: GHSV = 25,000 h^{-1}, 1000 ppm of NH_3, 1000 ppm of NO, 3% O_2 in N_2, 0.1 model soot/catalyst mass ratio).

structure after heating to 250 °C. On the other hand, the rate of reduction of NO was substantially lower for the nonstructured mixed oxide catalyst. As its surface area is higher than that of the 3DOM mixed oxide, the lower performance suggests that the surface of the nontemplated mixed oxide has a different composition, likely containing fewer Fe sites.

Temperature-programmed reduction (H_2-TPR) profiles of 3DOM $Ce_{0.9-x}Fe_xZr_{0.1}O_2$ catalysts demonstrate the better reducibility of the Fe-doped Ce−Zr mixed oxides compared with CeO_2 and Ce−Zr oxide (Figure 7). The 3DOM ceria

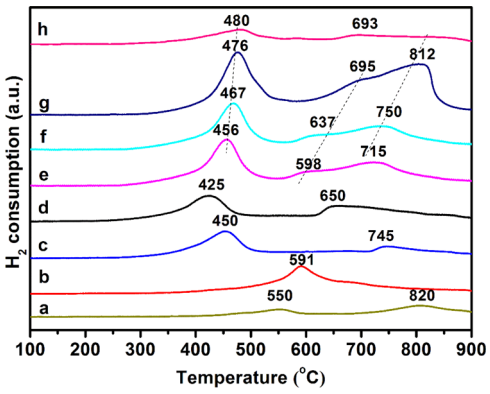

Figure 7. H_2-TPR traces of the 3DOM materials: (a) CeO_2, (b) $CeZrO_2$, (c) $Ce_{0.85}Fe_{0.05}Zr_{0.1}O_2$, (d) $Ce_{0.8}Fe_{0.1}Zr_{0.1}O_2$, (e) $Ce_{0.7}Fe_{0.2}Zr_{0.1}O_2$, (f) $Ce_{0.6}Fe_{0.3}Zr_{0.1}O_2$, and (g) $Ce_{0.5}Fe_{0.4}Zr_{0.1}O_2$, and (h) nontemplated $Ce_{0.8}Fe_{0.1}Zr_{0.1}O_2$.

sample shows two reduction maxima at 550 and 820 °C due to surface and bulk reduction. The mixed $CeZrO_2$ sample shows one reduction feature at 591 °C. Inclusion of Zr in the ceria lattice is known to increase the reducibility of the bulk of ceria.[64,65] An additional low-temperature reduction feature in the 425−476 °C range appears in the Fe-doped mixed oxides. It occurs at the lowest temperature for the best-performing $Ce_{0.8}Fe_{0.1}Zr_{0.1}O_2$ sample. The high-temperature reduction features observed for samples at higher Fe content are due to reduction of Fe_2O_3.[66,67] In line with the low NO SCR performance of the nontemplated mixed oxide, TPR shows that the surface reduction occurs at relatively high temperature and with relatively low hydrogen consumption. This suggests that a relatively small part of Fe is built into the ceria, indicating that the CMCCT method is conducive to generating highly dispersed Fe species in the ceria surface.

DFT Calculations. To better understand how doping with Fe enhances the reducibility of ceria and catalytic performance, we performed DFT + U calculations using a CeO_2 (111) surface model in which one Ce atom was substituted by an Fe atom. We choose the (111) surface, as it is the most stable termination of ceria. We studied the oxygen formation energy of Fe-doped ceria as well as a reaction mechanism for the oxidation of NO to N_2 by NH_3 and O_2. Finally, we also discuss the role of adsorbed O_2 in the oxidation of coke.

Compared with the high oxygen vacancy formation energy of the stoichiometric (111) surface of ceria (2.1 eV, 1 eV ≈ 96 kJ/mol), removing an oxygen atom from the Fe-doped CeO_2(111) surface is exothermic by −0.10 eV. This result implies that the ceria surface will already contain oxygen vacancies. The energy to remove a second O atom close to the first one is 1.39 eV, which is still substantially lower than the oxygen vacancy formation energy of the stoichiometric ceria surface. Thus, the first reduction feature observed in the H_2-TPR traces of the Fe-doped samples is because of the removal of a second O atom close to the Fe substitution. The DFT calculations predict that removing this O atom results in two Ce^{3+} surface atoms (Figure 8a). In keeping with this, XPS confirms that the Fe-containing samples contain more Ce^{3+} than the Fe-free reference sample (Table 2). The highest Ce^{3+}/Ce^{4+} ratio was observed for the most active sample. XPS also demonstrates that the surface contains the highest amount of surface adsorbed oxygen in the form of O_2^{2-} and O^-. We speculate that the oxygen species at higher binding energy are, because of molecular oxygen, strongly adsorbed on oxygen vacancies in close proximity to the Fe dopant in the ceria surface. DFT calculations show that molecular O_2 strongly adsorbs to the defective Fe-substituted ceria surface, forming O_2^{2-} species (E_{ads} = −0.71 eV, Figure 8b).

The combined results of surface characterization and catalytic testing emphasize the unique properties of Fe atoms doped into ceria toward NO reduction with NH_3 combined with soot oxidation. To gain better insight into the role of ceria doping with Fe, we investigated the mechanism of NO reduction by NH_3 through DFT calculations (Figure 9). We started the catalytic cycle from the stable surface under oxygen-rich conditions, i.e., the surface that contains O_2 adsorbed on the oxygen vacancy close to the Fe site (state i). NO strongly adsorbs on the exposed Lewis acid Fe site (state ii, ΔE_{ads} = −2.15 eV). The adsorbed NO molecule will easily react with a ceria lattice O atom to form nitrite (state iii). The activation barrier determined by the climbing image nudged elastic band method is 0.39 eV. Although state iii is slightly less stable than state ii, the formation of the nitrite species allows NH_3 to adsorb on the Lewis acid Fe site. This adsorption is strong with ΔE_{ads} = −1.14 eV (state iv). The formation of nitrite stores NO on the surface and alleviates the competition between NO and NH_3 for adsorption on the catalytic surface. This Langmuir−Hinshelwood mechanism is entropically favored over the Eley−Rideal alternative involving direct reaction of NO from the gas phase with a lattice O atom. NH_3-TPD confirms that ammonia

DOI: 10.1021/acscatal.6b03387
ACS Catal. 2017, 7, 3883−3892

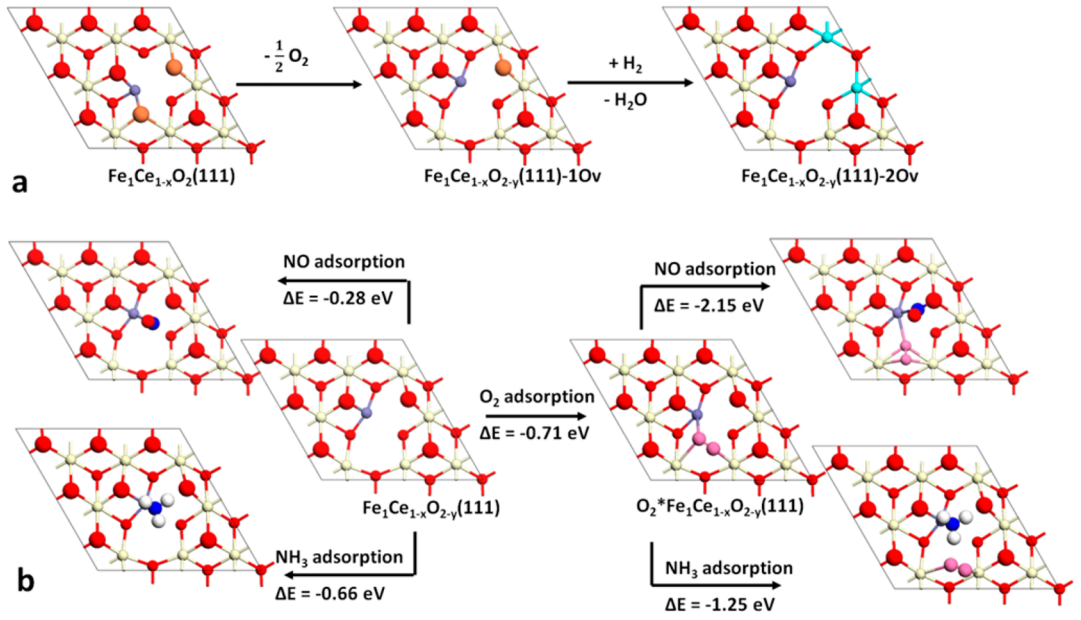

Figure 8. (a) Structure of Fe-doped $CeO_2(111)$ as the stoichiometric surface and with one and two oxygen vacancies; (b) adsorption of NH_3 and NO on Fe-doped $CeO_2(111)$ with one oxygen vacancy ($Fe_1Ce_{1-x}O_{2-y}(111)$); Fe-doped $CeO_2(111)$ with the oxygen vacancy preadsorbed by O_2 (O_2*$Fe_1Ce_{1-x}O_{2-y}(111)$). Color scheme: white, Ce^{4+}; green, Ce^{3+}; red, O; orange, O to be removed; purple, Fe; blue, N; bright white, H.

Table 2. Surface Composition and Oxidation State for the 3DOM Materials As Probed by XPS

	Ce 4f envelope			O 1s envelope			
				surface O		lattice O	
catalyst	Ce^{3+} (%)	Ce^{4+} (%)	Ce^{3+}/Ce^{4+}	O^-(%)	O_2^-(%)	O_2^-(%)	ratio[a]
$CeZrO_2$	21.1	78.9	0.267	7.4	19.4	73.2	0.366
$Ce_{0.85}Fe_{0.05}Zr_{0.1}O_2$	26	74.1	0.351	4.6	30.5	64.9	0.541
$Ce_{0.8}Fe_{0.1}Zr_{0.1}O_2$	26.3	73.7	0.357	4.7	30.7	64.6	0.548
$Ce_{0.7}Fe_{0.2}Zr_{0.1}O_2$	24.9	75.1	0.331	11.8	22.6	65.6	0.524
$Ce_{0.6}Fe_{0.3}Zr_{0.1}O_2$	23.5	76.5	0.307	8.9	23.8	67.3	0.486
$Ce_{0.5}Fe_{0.4}Zr_{0.1}O_2$	23	77	0.299	6.2	24.5	69.3	0.443

[a]Ratio of surface and lattice oxygen.

is more strongly adsorbed on the Fe-doped samples than on Fe-free samples (Figure S12).

An aspect worth discussing is that the adsorption of O_2 on the oxygen vacancy oxidizes Fe^{2+} to Fe^{3+}. Consequently, NH_3 adsorbs stronger on the surface in the presence of coadsorbed O_2 ($\Delta E_{ads,NH_3}$ = −1.25 eV) than in its absence ($\Delta E_{ads,NH_3}$ = −0.66 eV) (Figure 8b). Furthermore, NO adsorption is stronger on Fe^{3+} ($\Delta E_{ads,NO}$ = −2.15 eV) than on Fe^{2+} ($\Delta E_{ads,NO}$ = −0.28 eV) (Figure 8b). Both effects are expected to increase the rate of the NO SCR reaction.

The catalytic cycle continues by reaction of the nitrite species with adsorbed ammonia. First, one of the N−H bonds of chemisorbed NH_3 is activated by a basic O atom to form adsorbed OH and NH_2 surface species. Because of its higher basicity, H abstraction by a ceria lattice O^{2-} ion is preferred (state v, $\Delta E_{reaction}$ = 0.99 eV) over abstraction by coadsorbed O_2^{2-} (state v′ represented in Figure 9, $\Delta E_{reaction}$ = 1.55 eV). The resulting NH_2 radical will then react with NO to form $ONNH_2$ as a reactive intermediate. The activation barrier for this process is very low ($\Delta E_{barrier}$ = 0.21 eV). For the decomposition of this complex, we follow the mechanism identified in gas phase cluster studies of VO_3 and V_2O_5 with NO and NH_3.[68−70] By abstraction of another H atom and proton transfer from the OH group ($\Delta E_{reaction}$ = 0.92 eV), the HONNH surface intermediate is obtained, which weakly binds via its OH moiety to the Fe site (state vii, ΔE_{ads} = 0.20 eV). Such intermediates are very unstable[71] and decompose without activation barrier to gaseous N_2 and, in this case, two OH groups, one bridging between two Ce ions and one coordinating to the Fe cation (state viii). These reaction events are very exothermic ($\Delta E_{reaction}$ = −3.76 eV). The surface then contains three OH groups (the three H atoms originate from ammonia; the O atom is one of the OH groups from NO). One OH group and one proton are removed as water (state ix, ΔE_{des} = 1.4 eV). The proton left behind will remove an O atom from the surface as water together with another proton obtained in a subsequent similar reaction cycle. The energetics of subsequent cycles should be very similar to the above-described cycle.[72] Finally, the resulting O vacancies will be filled by dissociating O_2. Taken together, these reactions amount to the overall 4 NO + 4 NH_3 + O_2 → 4 N_2 + 6 H_2O reaction stoichiometry. The potential energy diagram for the formation of the first part of the cycle is shown in Figure 9. Candidate rate-controlling steps are the two proton abstraction steps (iv → v and vi → vii) and water desorption (ix → x), as the latter step is facilitated by the entropy gain of water desorbing from the surface. Therefore, the present data suggest that the proton abstraction steps from ammonia to the ceria

DOI: 10.1021/acscatal.6b03387
ACS Catal. 2017, 7, 3883−3892

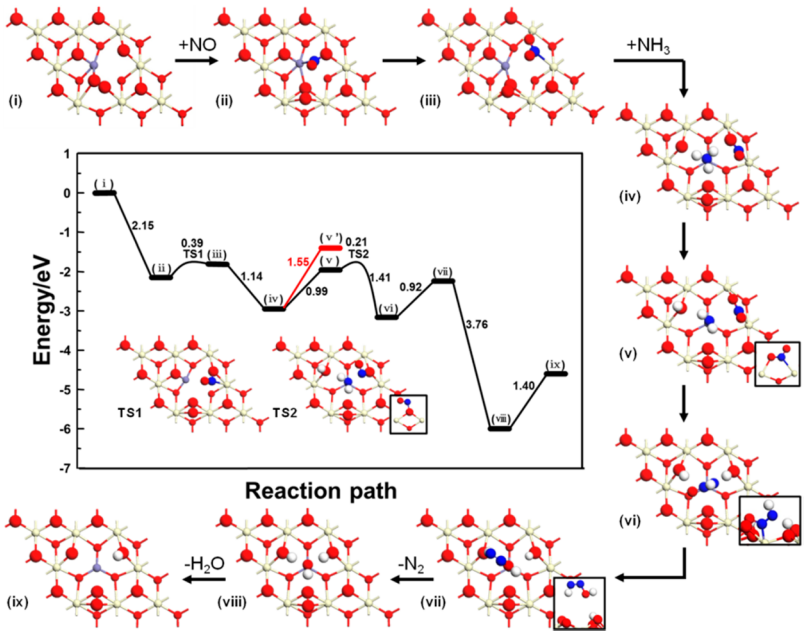

Figure 9. Potential energy diagram of NO reduction with key reaction intermediates. State v and v′ represent N−H dissociation in adsorbed NH_3 by lattice O and adsorbed O_2, respectively.

surface are the most likely reaction steps that control the overall reaction rate.

A second aspect of doping ceria with Fe relates to the oxidation of soot. Routine soot oxidation in CDPF is undergone before NO reduction because NO_2 produced by NO oxidation in the first step is a stronger oxidant than O_2. To evaluate the influence of NO removal during soot oxidation, we carried out a soot oxidation experiment without NO and NH_3 in the feed (Figure S13). The activity of the catalyst was slightly lower in this way, as evidenced by the small shift in the CO_2 production maximum to higher temperature (405 °C). Nevertheless, the performance of the $Ce_{0.8}Fe_{0.1}Zr_{0.1}O_2$ catalyst under these conditions was still outstanding compared to that of reference systems. This result implies that the substitution of Fe into the ceria surface leads to activated oxygen species that are involved in the oxidation of soot. Although a thorough computational analysis of these aspects is beyond the scope of this study, electronic analysis of adsorbed O_2 on the defective Fe-substituted ceria model (state i) and stoichiometric ceria shows nearly similar energetics with a formal O_2^- state. However, comparison of the density of states (Figure S14) shows more O 2p states close to the Fermi level for O_2 adsorbed on the defective Fe-substituted ceria model, which will enhance oxidation of aromatics. Another relevant aspect is the much higher density of O vacancies in Fe-doped ceria as compared with the stoichiometric ceria surface, which should also contribute significantly to the improved soot oxidation performance.

CONCLUSIONS

We demonstrate that 3DOM mixed Fe−Ce−Zr oxides are suitable for the simultaneous oxidation of soot and selective catalytic reduction of NO_x in SCRPF technology. NO is reduced by >90%, and soot is completely combusted in the 265−420 °C temperature range. The addition of Fe and Zr to ceria lowers the temperature of soot combustion to a level that is typically achieved by more expensive Pt catalysts. The 3DOM texture is suitable for trapping soot particles, and the presence of Fe in the ceria surface gives rise to high activity in NO_x reduction and soot oxidation at intermediate temperatures. The importance of the open macroporous 3DOM texture in soot capture and combustion was demonstrated by comparison to a mesoporous mixed oxide of the same composition. Surface characterization and DFT calculations show that substitution of Fe in the structured mixed Ce−Zr oxide increased the number of oxygen vacancies. A mechanism is explored for the reduction of NO with NH_3 involving adsorbed O_2 as a catalytic surface intermediate. Such adsorbed O_2 species may also be important in soot oxidation. These structured mixed oxides may find application in diesel particulate filters, e.g., by inclusion in wall flow filters constituting ceramic honeycomb structures plugged to force the exhaust flow through the walls. One may, for instance, consider integrating mixed oxide developed here with the base corderite ceramic used in such filters.

ASSOCIATED CONTENT

Supporting Information

The Supporting Information is available free of charge on the ACS Publications website at DOI: 10.1021/acscatal.6b03387.

Test for heat mass transfer limitations, XRD patterns, SEM images, and N_2 adsorption-desorption isotherms of 3DOM catalysts, NH_3 and NO conversion, XPS spectra, NH_3-TPD curves, projected density of states, average crystal grain sizes, and catalytic performance comparison (PDF)

AUTHOR INFORMATION

Corresponding Authors

*Tel: (+86) 10-89732778; e-mail: liujian@cup.edu.cn.
*Tel: (+86) 10-89732326; e-mail: zhaozhen@synu.edu.cn.
*Tel: (+31) 40-2455054; e-mail: E.J.M.Hensen@TUE.nl.

ORCID

Jian Liu: 0000-0003-3392-9812
Emiel J. M. Hensen: 0000-0002-9754-2417

DOI: 10.1021/acscatal.6b03387
ACS Catal. 2017, 7, 3883−3892

Author Contributions

[⊥]Y. C. and W. S. contributed equally to this work.

Notes

The authors declare no competing financial interest.

■ ACKNOWLEDGMENTS

This work was financially supported by the National Natural Science Foundation of China (21673290, 21503273, and U1662103) and the 863 Program (2015AA034603). E.J.M.H. acknowledges support of a VICI grant by The Netherlands Organization for Scientific Research.

■ REFERENCES

(1) Niessner, R. *Angew. Chem., Int. Ed.* **2014**, *53*, 12366−12379.
(2) Megarajan, S. K.; Rayalu, S.; Nishibori, M.; Teraoka, Y.; Labhsetwar, N. *ACS Catal.* **2015**, *5*, 301−309.
(3) Kimura, R.; Wakabayashi, J.; Elangovan, S. P.; Ogura, M.; Okubo, T. *J. Am. Chem. Soc.* **2008**, *130*, 12844−12845.
(4) Zhao, Y.; Hao, R.; Yuan, B.; Jiang, J. *J. Hazard. Mater.* **2016**, *301*, 74−83.
(5) Tsinoglou, D. N.; Koltsakis, G. C.; Peyton Jones, J. C. *Ind. Eng. Chem. Res.* **2002**, *41*, 1152−1165.
(6) Matarrese, R.; Morandi, S.; Castoldi, L.; Villa, P.; Lietti, L. *Appl. Catal., B* **2017**, *201*, 318−330.
(7) Teraoka, Y.; Kanada, K.; Kagawa, S. *Appl. Catal., B* **2001**, *34*, 73−78.
(8) Yoshida, K.; Makino, S.; Sumiya, S.; Muramatsu, G.; Helferich, R. Simultaneous reduction of NOx and particulate emissions from diesel engine exhaust. *SAE Technical Paper*, 1989.
(9) Teraoka, Y.; Shangguan, W.; Jansson, K.; Nygren, M.; Kagawa, S. *Bull. Chem. Soc. Jpn.* **1999**, *72*, 133−137.
(10) Zhang, H.-L.; Zhu, Y.; Wang, S.-D.; Zhao, M.; Gong, M.-C.; Chen, Y.-Q. *Fuel Process. Technol.* **2015**, *137*, 38−47.
(11) Liu, S.; Wu, X.; Weng, D.; Li, M.; Lee, H.-R. *Chem. Eng. J.* **2012**, *203*, 25−35.
(12) Parks, J. E. *Science* **2010**, *327*, 1584−1585.
(13) Cortés-Reyes, M.; Herrera, C.; Larrubia, M. Á.; Alemany, L. J. *Appl. Catal., B* **2016**, *193*, 110−120.
(14) Marberger, A.; Ferri, D.; Elsener, M.; Kröcher, O. *Angew. Chem., Int. Ed.* **2016**, *55*, 11989−11994.
(15) Wang, Z.; Yan, X.; Bi, X.; Wang, L.; Zhang, Z.; Jiang, Z.; Xiao, T.; Umar, A.; Wang, Q. *Mater. Res. Bull.* **2014**, *51*, 119−127.
(16) Raj, A.; Zainuddin, Z.; Sander, M.; Kraft, M. *Carbon* **2011**, *49*, 1516−1531.
(17) El Kadib, A.; Chimenton, R.; Sachse, A.; Fajula, F.; Galarneau, A.; Coq, B. *Angew. Chem.* **2009**, *121*, 5069−5072.
(18) Wei, Y.; Liu, J.; Zhao, Z.; Chen, Y.; Xu, C.; Duan, A.; Jiang, G.; He, H. *Angew. Chem., Int. Ed.* **2011**, *50*, 2326−2329.
(19) Peng, Q.; Zhao, H.; Qian, L.; Wang, Y.; Zhao, G. *Appl. Catal., B* **2015**, *174*−*175*, 157−166.
(20) Yang, C.; Yu, X.; Heißler, S.; Nefedov, A.; Colussi, S.; Llorca, J.; Trovarelli, A.; Wang, Y.; Wöll, C. *Angew. Chem., Int. Ed.* **2017**, *56*, 2−2.
(21) Rout, K. R.; Fenes, E.; Baidoo, M. F.; Abdollahi, R.; Fuglerud, T.; Chen, D. *ACS Catal.* **2016**, *6*, 7030−7039.
(22) Cargnello, M.; Jaén, J. D.; Garrido, J. H.; Bakhmutsky, K.; Montini, T.; Gámez, J. C.; Gorte, R.; Fornasiero, P. *Science* **2012**, *337*, 713−717.
(23) Gao, Y.; Wu, X.; Liu, S.; Weng, D.; Zhang, H.; Ran, R. *Catal. Today* **2015**, *253*, 83−88.
(24) Liu, J.; Zhao, Z.; Wang, J.; Xu, C.; Duan, A.; Jiang, G.; Yang, Q. *Appl. Catal., B* **2008**, *84*, 185−195.
(25) Giménez-Mañogil, J.; Bueno-López, A.; García-García, A. *Appl. Catal., B* **2014**, *152*−*153*, 99−107.
(26) Neyertz, C. A.; Banús, E. D.; Miró, E. E.; Querini, C. A. *Chem. Eng. J.* **2014**, *248*, 394−405.
(27) Atribak, I.; Buenolopez, A.; Garciagarcia, A. *J. Catal.* **2008**, *259*, 123−132.
(28) Cai, S.; Zhang, D.; Zhang, L.; Huang, L.; Li, H.; Gao, R.; Shi, L.; Zhang, J. *Catal. Sci. Technol.* **2014**, *4*, 93−101.
(29) Arandiyan, H.; Dai, H.; Ji, K.; Sun, H.; Li, J. *ACS Catal.* **2015**, *5*, 1781−1793.
(30) Yu, J.; Si, Z.; Chen, L.; Wu, X.; Weng, D. *Appl. Catal., B* **2015**, *163*, 223−232.
(31) Wei, Y.; Liu, J.; Zhao, Z.; Duan, A.; Jiang, G.; Xu, C.; Gao, J.; He, H.; Wang, X. *Energy Environ. Sci.* **2011**, *4*, 2959−2970.
(32) Trasobares, S.; López-Haro, M.; Kociak, M.; March, K.; de La Peña, F.; Perez-Omil, J. A.; Calvino, J. J.; Lugg, N. R.; D'Alfonso, A. J.; Allen, L. J. *Angew. Chem., Int. Ed.* **2011**, *50*, 868−872.
(33) Aneggi, E.; de Leitenburg, C.; Dolcetti, G.; Trovarelli, A. *Catal. Today* **2006**, *114*, 40−47.
(34) Li, G.; Smith, R. L.; Inomata, H. *J. Am. Chem. Soc.* **2001**, *123*, 11091−11092.
(35) Xu, J.; Liu, J.; Zhao, Z.; Xu, C.; Zheng, J.; Duan, A.; Jiang, G. *J. Catal.* **2011**, *282*, 1−12.
(36) Zhang, G.; Zhao, Z.; Xu, J.; Zheng, J.; Liu, J.; Jiang, G.; Duan, A.; He, H. *Appl. Catal., B* **2011**, *107*, 302−315.
(37) Cao, X.; Zheng, B.; Rui, X.; Shi, W.; Yan, Q.; Zhang, H. *Angew. Chem., Int. Ed.* **2014**, *53*, 1404−1409.
(38) Qin, D.; Cadet, G. *Anal. Chem.* **1997**, *69*, 1942−1945.
(39) Perdew, J. P.; Burke, K.; Ernzerhof, M. *Phys. Rev. Lett.* **1996**, *77*, 3865.
(40) Blöchl, P. E. *Phys. Rev. B: Condens. Matter Mater. Phys.* **1994**, *50*, 17953.
(41) Kresse, G.; Joubert, D. *Phys. Rev. B: Condens. Matter Mater. Phys.* **1999**, *59*, 1758.
(42) Da Silva, J. L. F.; Ganduglia-Pirovano, M. V.; Sauer, J.; Bayer, V.; Kresse, G. *Phys. Rev. B: Condens. Matter Mater. Phys.* **2007**, *75*, 045121−045110.
(43) Fabris, S.; de Gironcoli, S.; Baroni, S.; Vicario, G.; Balducci, G. *Phys. Rev. B: Condens. Matter Mater. Phys.* **2005**, *72*, 237102.
(44) Cococcioni, M.; de Gironcoli, S. *Phys. Rev. B: Condens. Matter Mater. Phys.* **2005**, *71*, 035105−035116.
(45) Castleton, C.; Kullgren, J.; Hermansson, K. *J. Chem. Phys.* **2007**, *127*, 244704−244704.
(46) Huang, X.; Ramadugu, S. K.; Mason, S. E. *J. Phys. Chem. C* **2016**, *120*, 4919−4930.
(47) Henkelman, G.; Uberuaga, B. P.; Jónsson, H. *J. Chem. Phys.* **2000**, *113*, 9901−9904.
(48) Orilall, M. C.; Abrams, N. M.; Lee, J.; DiSalvo, F. J.; Wiesner, U. *J. Am. Chem. Soc.* **2008**, *130*, 8882−8883.
(49) Yang, J.; Yang, Z.; Wang, Y.; Li, J.; Shao, B.; Qiu, J.; Song, Z.; Frenc, R. H. *J. Am. Ceram. Soc.* **2015**, *98*, 2011−2013.
(50) Magnacca, G.; Cerrato, G.; Morterra, C.; Signoretto, M.; Somma, F.; Pinna, F. *Chem. Mater.* **2003**, *15*, 675−687.
(51) Zhan, S.; Zhang, H.; Zhang, Y.; Shi, Q.; Li, Y.; Li, X. *Appl. Catal., B* **2017**, *203*, 199−209.
(52) dos Santos Xavier, L. P.; Rico-Pérez, V.; Hernández-Giménez, A. M.; Lozano-Castelló, D.; Bueno-López, A. *Appl. Catal., B* **2015**, *162*, 412−419.
(53) Perry, R. A.; Siebers, D. L. *Nature* **1986**, *324*, 657−658.
(54) Boubnov, A.; Carvalho, H. W.; Doronkin, D. E.; Gunter, T.; Gallo, E.; Atkins, A. J.; Jacob, C. R.; Grunwaldt, J. D. *J. Am. Chem. Soc.* **2014**, *136*, 13006−13015.
(55) Heylen, S.; Delcour, N.; Kirschhock, C. E. A.; Martens, J. A. *ChemCatChem* **2012**, *4*, 1162−1166.
(56) Liu, Z.; Wakihara, T.; Oshima, K.; Nishioka, D.; Hotta, Y.; Elangovan, S. P.; Yanaba, Y.; Yoshikawa, T.; Chaikittisilp, W.; Matsuo, T.; Takewaki, T.; Okubo, T. *Angew. Chem., Int. Ed.* **2015**, *54*, 5683−5687.
(57) Paolucci, C.; Verma, A. A.; Bates, S. A.; Kispersky, V. F.; Miller, J. T.; Gounder, R.; Delgass, W. N.; Ribeiro, F. H.; Schneider, W. F. *Angew. Chem., Int. Ed.* **2014**, *53*, 11828−11833.
(58) Mou, X.; Zhang, B.; Li, Y.; Yao, L.; Wei, X.; Su, D. S.; Shen, W. *Angew. Chem., Int. Ed.* **2012**, *51*, 2989−2993.
(59) Shan, W.; Liu, F.; He, H.; Shi, X.; Zhang, C. *Chem. Commun.* **2011**, *47*, 8046−8048.

DOI: 10.1021/acscatal.6b03387
ACS Catal. 2017, 7, 3883−3892

(60) Li, J.; Zhu, R.; Cheng, Y.; Lambert, C. K.; Yang, R. T. *Environ. Sci. Technol.* **2010**, *44*, 1799−1805.
(61) Liu, S.; Wu, X.; Weng, D.; Li, M.; Ran, R. *ACS Catal.* **2015**, *5*, 909−919.
(62) Wang, H.; Qu, Z.; Xie, H.; Maeda, N.; Miao, L.; Wang, Z. *J. Catal.* **2016**, *338*, 56−67.
(63) Kureti, S.; Weisweiler, W.; Hizbullah, K. *Appl. Catal., B* **2003**, *43*, 281−291.
(64) Wang, H.-F.; Gong, X.-Q.; Guo, Y.-L.; Guo, Y.; Lu, G. Z.; Hu, P. *J. Phys. Chem. C* **2009**, *113*, 10229−10232.
(65) Mayernick, A. D.; Janik, M. J. *J. Phys. Chem. C* **2008**, *112*, 14955−14964.
(66) Kim, H. Y.; Lee, H. M.; Henkelman, G. *J. Am. Chem. Soc.* **2012**, *134*, 1560−1570.
(67) Zhang, Z.; Han, D.; Wei, S.; Zhang, Y. *J. Catal.* **2010**, *276*, 16−23.
(68) Walch, S. P. *J. Chem. Phys.* **1993**, *99*, 5295−5300.
(69) Duan, X.; Page, M. *J. Mol. Struct.: THEOCHEM* **1995**, *333*, 233−242.
(70) Soyer, S.; Uzun, A.; Senkan, S.; Onal, I. *Catal. Today* **2006**, *118*, 268−278.
(71) Phillips, L. *Chem. Phys. Lett.* **1987**, *135*, 269−274.
(72) Song, W.; Liu, J.; Zheng, H.; Ma, S.; Wei, Y.; Duan, A.; Jiang, G.; Zhao, Z.; Hensen, E. J. *Catal. Sci. Technol.* **2016**, *6*, 2120−2128.

DOI: 10.1021/acscatal.6b03387
ACS Catal. 2017, 7, 3883−3892